ARTICLES
https://doi.org/10.1038/s41566-020-0618-9

nature photonics

Terahertz topological photonics for on-chip communication

Yihao Yang[1,2], Yuichiro Yamagami[3], Xiongbin Yu[3], Prakash Pitchappa[1,2], Julian Webber[3], Baile Zhang[1,2], Masayuki Fujita[3] ✉, Tadao Nagatsuma[3] and Ranjan Singh[1,2] ✉

The realization of integrated, low-cost and efficient solutions for high-speed, on-chip communication requires terahertz-frequency waveguides and has great potential for information and communication technologies, including sixth-generation (6G) wireless communication, terahertz integrated circuits, and interconnects for intrachip and interchip communication. However, conventional approaches to terahertz waveguiding suffer from sensitivity to defects and sharp bends. Here, building on the topological phase of light, we experimentally demonstrate robust terahertz topological valley transport through several sharp bends on the all-silicon chip. The valley kink states are excellent information carriers owing to their robustness, single-mode propagation and linear dispersion. By leveraging such states, we demonstrate error-free communication through a highly twisted domain wall at an unprecedented data transfer rate (exceeding ten gigabits per second) that enables real-time transmission of uncompressed 4K high-definition video (that is, with a horizontal display resolution of approximately 4,000 pixels). Terahertz communication with topological devices opens a route towards terabit-per-second datalinks that could enable artificial intelligence and cloud-based technologies, including autonomous driving, healthcare, precision manufacturing and holographic communication.

Terahertz (THz) waves have frequencies extending from 0.1 THz to 10 THz that fall between microwaves and optical waves: a region known as the 'THz gap' owing to the lack of many functional devices in this frequency range[1–16]. The THz spectral region offers a higher available bandwidth, which could meet the ever-growing demand for higher data transfer rates[11,15]. The THz spectral band is key to the development of 6G mobile communication networks, which need to be able to transmit data wirelessly at terabits per second over a distance of kilometres; it could also enable the implementation of the 'internet of things', with a network of over a trillion communicating devices. The THz spectral band may also be used to address the long-standing interconnect issue of achieving high-speed, energy-efficient and low-cost intrachip/interchip communication links over a range of a few centimetres to realize massive multicore processors, network-on-chip or system-in-package solutions[17–22]. To achieve these goals, we need integrated, low-cost, efficient solutions for on-chip THz waveguiding and manipulation. Conventional approaches to THz waveguiding include hollow metallic waveguides[4], metallic transmission lines[1], photonic crystals[10], metal wires[5] and THz fibres[7]. However, such conventional approaches suffer from sensitivity to defects such as fabrication imperfections and considerable bending losses at sharp corners.

The recent discovery of the topological phase of light[23–27] has suggested possible solutions to the above problem. For example, photonic topological insulators (PTIs)[23,25,27], which are 'insulating' in bulk but 'conducting' at the edges, show robust edge transport with strongly suppressed backscattering caused by disorder and sharp bends. Much effort has been devoted to investigating spin-Hall PTIs[28–32] and valley Hall PTIs (also known as valley Hall photonic crystals, VPCs)[33–39], which exhibit time-reversal symmetry and do not require magnetic components or temporal modulation. The PTIs already show excellent potential for applications in modern optical devices such as reflectionless waveguides[40], topological quantum interfaces[41], topological light sources[42], topological lasers[43–45], topological splitters[31] and robust delay lines[46]. However, at present, experimental studies on PTIs have been largely limited to the microwave[29,31,32,34,36,40,47] and optical frequencies[28,37,38,41–45,48], while the THz PTI experiments have been limited by the material platforms and characterization tools available for the THz spectral region.

Here, building on the topological phase of light, we experimentally demonstrate robust THz topological valley transport on an all-silicon chip. To the best of our knowledge, this is the first experimental demonstration of the topological phase of THz waves. Silicon-platform-based on-chip VPCs have the additional merit of being extremely low loss, which is highly desirable in future THz integrated circuits and THz communications. In our experiments, we unambiguously demonstrate that valley-polarized topological kink states are very robust and exhibit near-unity transmission over a bulk bandgap, even after propagating through ten sharp bends with zero radii of curvature, which includes five 120° bends and five 60° bends. Topological valley kink states are promising for THz communication because of their robustness, single-mode and linear-dispersion properties. As a proof of concept, we experimentally demonstrate error-free communication through a VPC with a highly twisted domain wall at a high data transfer rate in addition to the successful transmission of uncompressed 4K high-definition video.

Results

Design of on-chip THz VPCs. The THz VPCs are patterned on high-resistivity (>10 kΩ cm) silicon (of relative permittivity 11.7) chips with a thickness of $h = 190\,\mu m$, as depicted in Fig. 1a. The VPC design follows the well known graphene-like lattice with

---

[1]Division of Physics and Applied Physics, School of Physical and Mathematical Sciences, Nanyang Technological University, Singapore, Singapore. [2]Centre for Disruptive Photonic Technologies, The Photonics Institute, Nanyang Technological University, Singapore, Singapore. [3]Graduate School of Engineering Science, Osaka University, Toyonaka, Japan. ✉e-mail: fujita@ee.es.osaka-u.ac.jp; ranjans@ntu.edu.sg

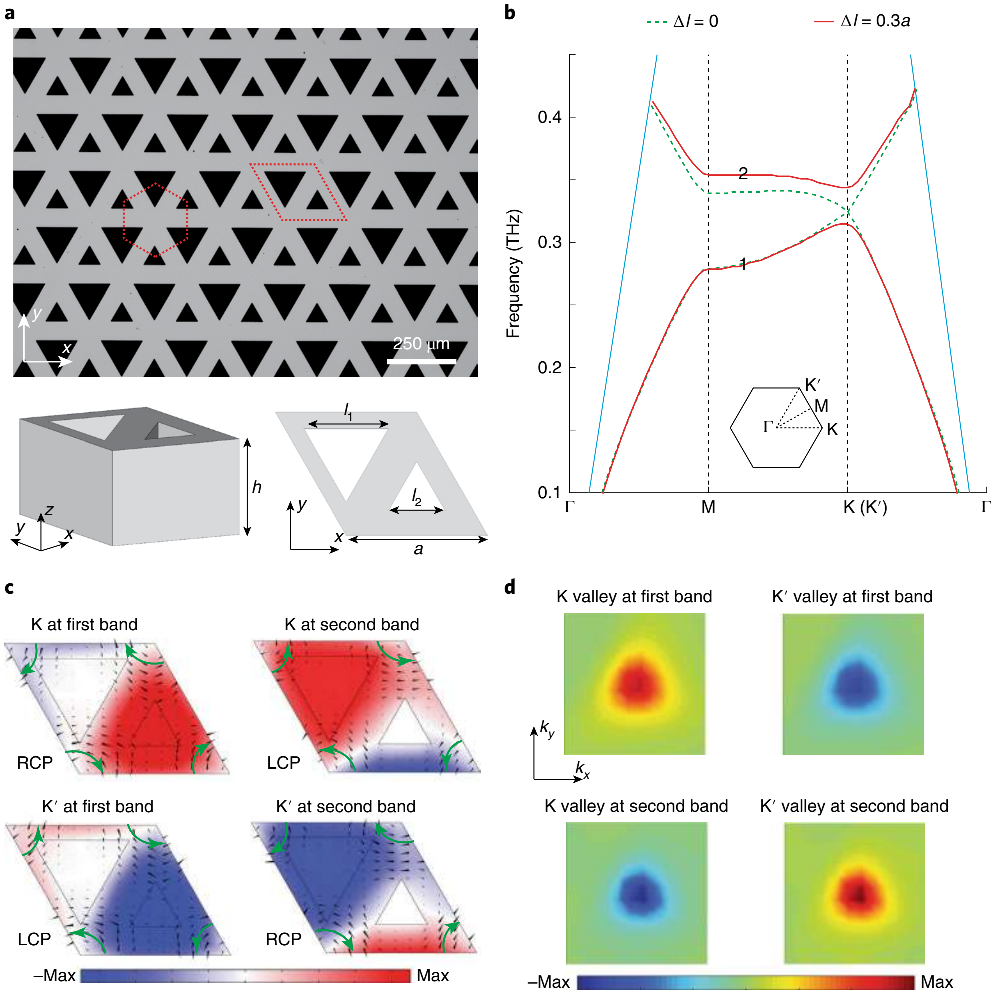

Fig. 1 | On-chip THz VPC and its bulk band diagram. **a**, An optical image of the fabricated sample. The red dashed lines show Wigner–Seitz and unit cells. Magnified views of the unit cell are presented below the optical image. **b**, Band diagrams with and without inversion symmetry. The green, red and blue lines represent the dispersion of the VPC with and without inversion symmetry, and the light line of air, respectively. **c**, Mode profiles at the K and K′ valleys for the first and second bands of the VPC. The colour scale shows the *z*-oriented magnetic field H_z, while black and green arrows denote the Poynting power flow. **d**, Normalized simulated Berry curvatures near the K and K′ valleys for both bands. The plotted range for each inset is $[-0.33\pi/a, 0.33\pi/a]^2$, centred at the K or K′ valleys.

lattice constant $a = 242.5$ µm. Each unit cell comprises an equilateral triangular hole with a side length of l_1 and another inverted equilateral triangular hole with a side length of l_2. Here we focus on transverse-electric modes, where electric fields lie within the plane. The modes propagate in the *x*–*y* plane but are confined in the *z* direction owing to total internal reflection[49]. In the presence of inversion symmetry (for example, $l_1 = l_2 = 0.5a$), our VPC possesses C_6 symmetry that leads to a pair of degenerate Dirac points (at the K and K′ valleys) in the band diagram at 0.33 THz (Fig. 1b). Upon breaking the inversion symmetry (for example, $l_1 = 0.65a$ and $l_2 = 0.35a$), the VPC structure reduces to C_3 symmetry, resulting in the lifting of degeneracy and the disappearance of Dirac points. More importantly, inversion symmetry breaking opens a bandgap ($0.32\,\text{THz} < f < 0.35\,\text{THz}$) near the Dirac frequency (Fig. 1b). The distribution of the *z*-oriented magnetic field H_z and Poynting power flow of the modes at the K (K′) valley for both bands are shown in Fig. 1c). It can clearly be seen that there are four modes that exhibit either left-handed circular polarization (LCP) or right-handed circular polarization (RCP). Also, within the same band, the polarization of a mode at K′ is opposite to that of a mode at K.

It is known that the VPCs feature nonzero Berry curvatures localized at the K and K′ valleys[34,36,37,50]. We calculate Berry curvatures using a first-principles numerical method. Indeed, we find nonzero Berry curvatures localized around different valleys (Fig. 1d). Additionally, within the same band, these Berry curvatures are identical but opposite in sign for the K and K′ valleys. Therefore, the total Berry curvature of any single band is zero. This is also guaranteed by the preservation of time-reversal symmetry in our VPC. Integrating Berry curvatures around different valleys, we further find that the valley Chern numbers are half-integers, that is, $C_K = 1/2$ and $C_{K'} = -1/2$ for the first band and $C_K = -1/2$ and $C_{K'} = 1/2$ for the second band. Our numerical results are consistent with previous work in the optical and microwave regimes[34,36,38].

To visualize the valley Hall topological phase transition, we numerically obtain the evolution of eigenfrequencies at the K valley for both bands as a function of Δl ($\Delta l = l_1 - l_2$) (Fig. 2a). As shown in Fig. 2a, the obtained results confirm that the polarization of the states is flipped in the phase diagram when Δl crosses zero. On the left side, LCP is below and RCP is above ($\Delta l < 0$) in Fig. 2a, but on the right side, the polarization flips to LCP above and RCP below ($\Delta l > 0$). This inversion indicates that there are two topologically

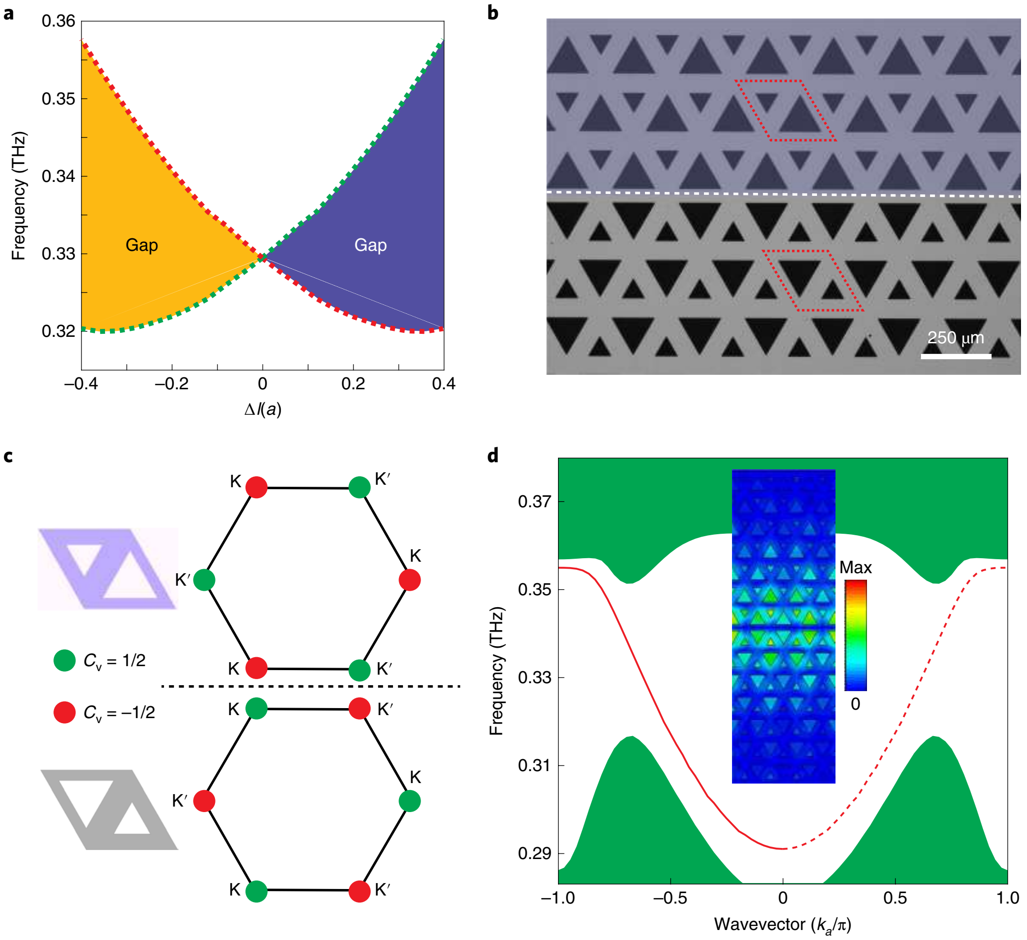

Fig. 2 | Phase diagram and topological valley kink states at the domain wall. a, A phase diagram showing the variation of the gap as a function of Δl in the range $-0.4a$ to $0.4a$. The green and red dotted lines represent LCP and RCP, respectively. **b**, An optical image of the fabricated domain wall with opposite Δl on each side. The white dashed line represents the interface between two domains. **c**, Topological charge distribution and valley Chern number (C_v) on each side of the domain wall. The dashed line denotes the domain wall. **d**, Dispersion of topological kink states at the domain wall. The red line and the green regions represent the edge dispersion and the projected bulk dispersion, respectively. The inset shows the intensity distribution (colour scale) of the magnetic field around the domain wall. The red dashed and solid lines represent the kink states locked to the K and K′ valleys, respectively. k_a denotes the wavevector along the domain wall.

different valley Hall phases directly related to the sign of Δl. Our numerical calculations further show that the valley Chern numbers for these two valley Hall phases are exactly opposite.

Next, as shown in Fig. 2b, we construct a 'kink'-type domain wall between two VPCs with opposite Δl values. The difference of the valley Chern numbers across the domain wall at the K (K′) valley is $C_\Delta = \pm 1$ (Fig. 2c). According to the bulk-boundary correspondence, a pair of valley-polarized topological kink states appear at the domain wall within the bandgap: one locked to the K valley propagates forward, while the other one, locked to the K′ valley, propagates backward. As shown in Fig. 2d, our simulation results are consistent with this prediction. Interestingly, the dispersion of valley kink states is almost linear in the bandgap, which can be explained using the effective two-dimensional massive Dirac Hamiltonian model[50] (Methods). Furthermore, there is only a single kink state in the bandgap for a certain wavevector owing to the condition $|C_\Delta| = 1$. The linear-dispersion and single-mode properties of valley kink states are advantageous for THz communication. The linear dispersion indicates a negligible signal delay at different frequencies, which enables a larger bandwidth[7]. On the other hand, the single-mode feature precludes mode competition and provides additional advantages similar to those of a single-mode optical fibre[51]. Besides, it has been revealed that the valley kink states are generally robust against fabrication imperfections, as long as these defects do not couple the states of the different valleys[38,39,52]. Therefore, the present design has substantial advantages in comparison to the other existing THz waveguides (Supplementary Information). It is also worth noting that the relative size of the VPC bandgap can be tuned by changing the Δl parameter (Fig. 2a), and the operational frequency of the VPC can be tuned by a simple scaling of the unit cell.

Experimental demonstration of robust topological valley kink states in a THz photonic chip. One of the most intriguing properties of topological valley kink states is that they are immune to sharp corners in the absence of inter-valley scattering[33,34,36,38,50]. To demonstrate this property, as shown in Fig. 3a, we fabricate a highly twisted domain wall on a 26 × 8 mm^2 silicon chip with ten sharp corners (with zero radii of curvature) including five 120° turns and five 60° turns. To experimentally measure the transmission of topological kink states along the twisted domain wall, we set up an experiment, as shown in Fig. 3b. The transmission is measured using an electronic-based continuous-wave THz spectrometer in a frequency range between 0.30 THz and 0.37 THz (Methods).

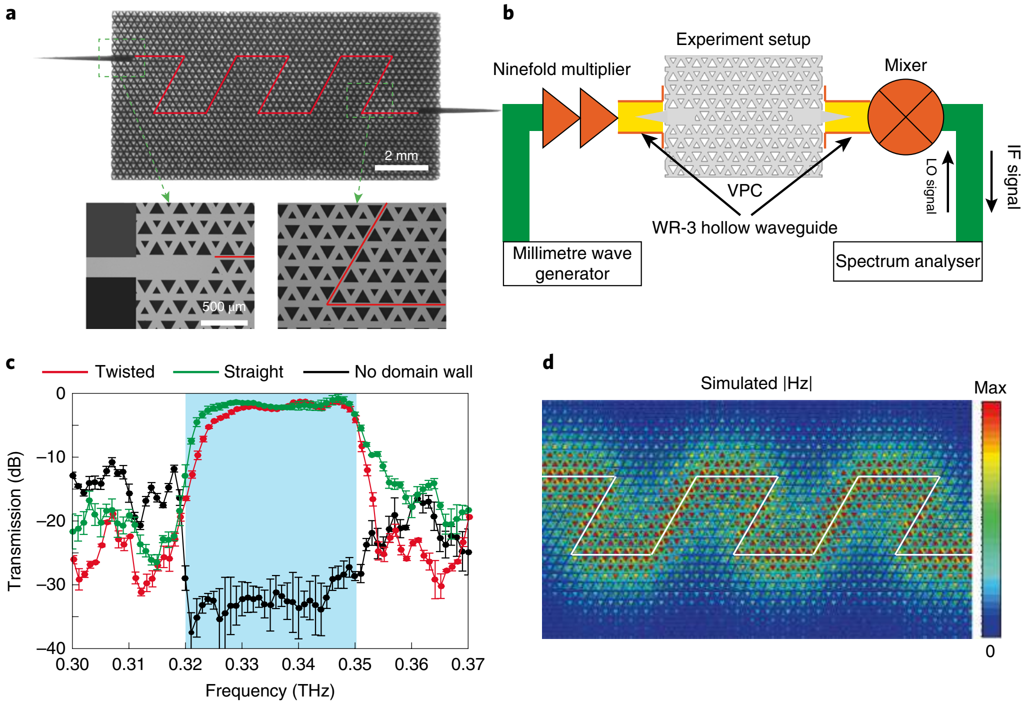

Fig. 3 | Experimental observation of robust topological valley kink states along a twisted domain wall in a large-scale THz photonic chip. a, An optical image of the fabricated twisted domain wall. The red lines represent the position of the domain walls. **b**, The experimental setup for measuring transmission. **c**, Measured transmission curves for a VPC with a straight domain wall, a twisted domain wall with ten corners and no domain wall. The error bars are derived from the standard deviation. The blue region represents the bulk bandgap. **d**, Simulated $|H_z|$ field distribution (colour scale) in the on-chip VPC at 0.335 THz. The white line denotes the position of the domain wall. IF, intermediate frequency; LO, local oscillator.

As shown in Fig. 3c, the measured results are compared with the transmission in VPCs comprising either a straight domain wall or no domain wall. A distinct dip in transmission, between 0.32 THz and 0.35 THz, can be clearly seen in a VPC without a domain wall, indicating the presence of a bulk bandgap. In contrast, the transmission within the bandgap is close to unity for VPCs with a twisted or straight domain wall. The minimum bending loss is estimated to be <0.1 dB per bend, which is smaller than that of a conventional THz photonic-crystal waveguide (about 0.2 dB per bend)[10]. However, outside the bandgap region, the transmission becomes complex and shows a noisy behaviour[34,36], owing to the reflection and refraction of the THz wave at the boundaries of the VPC and at the domain wall. We also perform full-wave simulations to compare the measured transmission curves for all three cases (see the simulated transmission in Supplementary Information) and to visualize the intensity distribution of the magnetic field near the twisted domain wall, as shown in Fig. 3d. It is evident that a kink state smoothly travels through sharp corners with negligible reflection. These results prove that the topological kink states are immune to sharp bends in our THz topological photonic chips.

Topological valley kink states for THz communications. Topological kink states can thus be excellent information carriers for on-chip THz communication, and hence may enable future 6G wireless networks. To further demonstrate this application, we performed the THz communication experiment using a highly twisted domain wall with ten sharp corners (Methods). The measured bit error rate as a function of the data transfer rate is shown in Fig. 4a. Clearly, we achieve an error-free (bit error rate $< 10^{-11}$) transmission at a data transfer rate of up to 11 Gbit s^{-1} with a carrier frequency of 0.335 THz. Remarkably, the bit rate of 11 Gbit s^{-1} that we achieve is higher than that of a conventional THz photonic crystal with bends or turns (1.5 Gbit s^{-1})[10]. Additionally, a clear eye diagram obtained on the screen of the oscilloscope at a data transfer rate of 11 Gbit s^{-1} is shown in Fig. 4b. We note that the maximum data transfer rate is mainly limited by the effective bandwidth of the VPC waveguide in the current system based on an on–off-keying modulation. Besides, the data transfer rate can be further enhanced by employing a phase modulator and a mixer receiver, applying higher-order multilevel modulation schemes[53], enhancing the relative bandwidth of the VPC, and increasing the carrier frequency. As an example, we achieve a data transfer rate of 16 Gbit s^{-1} within the forward error-correction limit (bit error rate $<1.84\times10^{-3}$) based on 16-quadrature amplitude modulation (Supplementary Information).

To demonstrate the capability of high-speed and high-quality real-time data transmission, as shown in Fig. 4c, we set up another experiment for transmitting an uncompressed 4K high-definition video at a data transfer rate of 6 Gbit s^{-1} (Methods). The transmitted 4K high-definition video is shown on the monitor in the background. From Fig. 4c and Supplementary Video 1, it can be seen that the 4K high-definition video is successfully transmitted in real-time through the VPC even with a twisted domain wall. All the above experiments unambiguously demonstrate that topological valley kink states are robust information carriers for on-chip THz communication.

Conclusions

We thus experimentally demonstrate robust photonic transport in low-loss silicon chip using the valley Hall topological phase of THz waves. Further, topological valley kink states are excellent information carriers for THz communication. By combining robust topological transport across sharp corners, single-mode propagation, and linear-dispersion of kink states, we experimentally demonstrate the error-free transmission of uncompressed 4K high-definition video to showcase the huge potential of THz topological photonics.

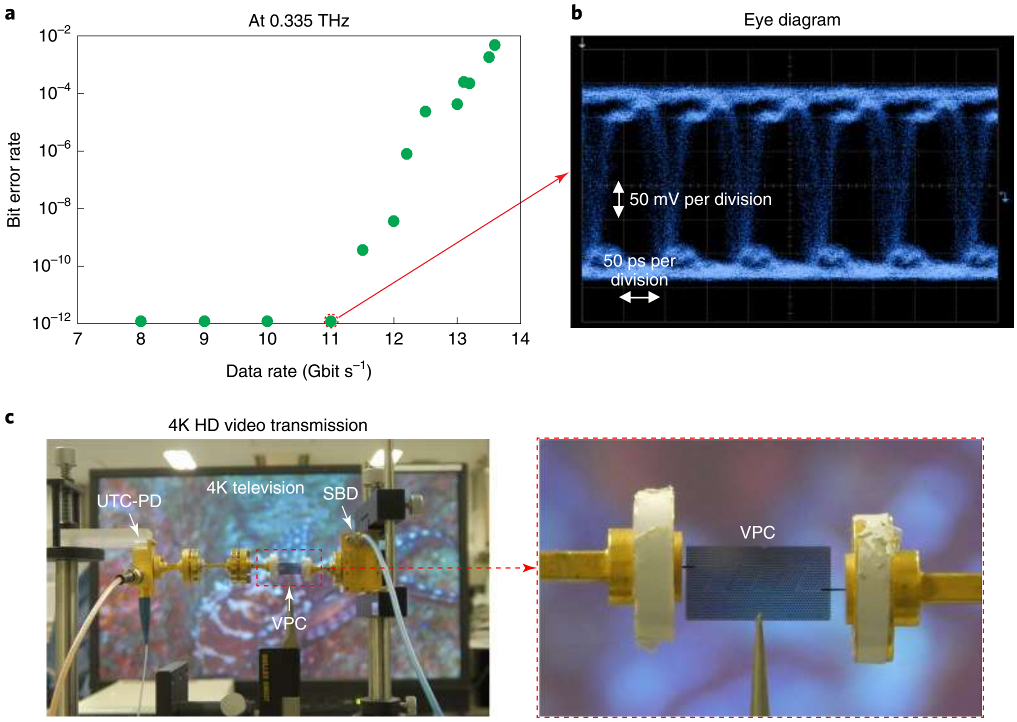

Fig. 4 | Terahertz communication based on robust topological valley transport. a, The measured bit error rate as a function of the data transfer rate at 0.335 THz. **b**, An eye diagram on the oscilloscope at 11 Gbit s^{-1} with a bit error rate of 1×10^{-12}. **c**, An experimental demonstration of uncompressed 4K high-definition video transmission. The transmitted 4K high-definition video is shown on the monitor in the background. The dashed red rectangle highlights the VPC with a twisted domain wall. An enlarged picture of the sample is shown on the right. SBD, Schottky barrier diode. UTC-PD, uni-travelling-carrier photodiode.

Topological kink states are poised to enable THz functional components such as topological splitters[31], robust delay lines[46], compact interferometers, and directional antennas[36,54] using low-loss and all-silicon VPC chips. Therefore, the present silicon-based VPC would serve as an ideal platform for the next generation of THz-wave integrated circuits and THz wireless communication (see a demonstration of uncompressed 4K high-definition wireless transmission based on our VPC chip in Supplementary Video 2). Finally, our work provides an experimental demonstration of the topological phases of a THz wave, which could inspire research on different types of topological phase in both two and three dimensions, including spin-Hall PTIs[41], quantum-Hall PTIs[40,43] and Weyl points[55–57], and related applications in THz sensing, imaging, spectroscopy and 6G mobile communications.

Online content

Any methods, additional references, Nature Research reporting summaries, source data, extended data, supplementary information, acknowledgements, peer review information; details of author contributions and competing interests; and statements of data and code availability are available at https://doi.org/10.1038/s41566-020-0618-9.

Received: 8 July 2019; Accepted: 2 March 2020;
Published online: 13 April 2020

References

1. Frankel, M. Y., Gupta, S., Valdmanis, J. A. & Mourou, G. A. Terahertz attenuation and dispersion characteristics of coplanar transmission lines. *IEEE Trans. Microw. Theory Tech.* **39**, 910–916 (1991).
2. Ferguson, B. & Zhang, X.-C. Materials for terahertz science and technology. *Nat. Mater.* **1**, 26–33 (2002).
3. Siegel, P. H. Terahertz technology in biology and medicine. *IEEE Trans. Microw. Theory Tech.* **52**, 2438–2447 (2004).
4. Harrington, J. A., George, R., Pedersen, P. & Mueller, E. Hollow polycarbonate waveguides with inner Cu coatings for delivery of terahertz radiation. *Opt. Express* **12**, 5263–5268 (2004).
5. Wang, K. & Mittleman, D. M. Metal wires for terahertz wave guiding. *Nature* **432**, 376–379 (2004).
6. Tonouchi, M. Cutting-edge terahertz technology. *Nat. Photon.* **1**, 97–105 (2007).
7. Atakaramians, S., Afshar, S., Monro, T. M. & Abbott, D. Terahertz dielectric waveguides. *Adv. Opt. Photon.* **5**, 169–215 (2013).
8. Mittleman, D. M. Frontiers in terahertz sources and plasmonics. *Nat. Photon.* **7**, 666–669 (2013).
9. Kakimi, R., Fujita, M., Nagai, M., Ashida, M. & Nagatsuma, T. Capture of a terahertz wave in a photonic-crystal slab. *Nat. Photon.* **8**, 657–663 (2014).
10. Tsuruda, K., Fujita, M. & Nagatsuma, T. Extremely low-loss terahertz waveguide based on silicon photonic-crystal slab. *Opt. Express* **23**, 31977–31990 (2015).
11. Nagatsuma, T., Ducournau, G. & Renaud, C. C. Advances in terahertz communications accelerated by photonics. *Nat. Photon.* **10**, 371–379 (2016).
12. Zhang, Q. et al. Collective non-perturbative coupling of 2D electrons with high-quality-factor terahertz cavity photons. *Nat. Phys.* **12**, 1005–1011 (2016).
13. Wang, X. et al. Topological-insulator-based terahertz modulator. *Sci. Rep.* **7**, 13486 (2017).
14. Mittleman, D. M. Twenty years of terahertz imaging. *Opt. Express* **26**, 9417–9431 (2018).
15. Ma, J. et al. Security and eavesdropping in terahertz wireless links. *Nature* **563**, 89–93 (2018).
16. Sengupta, K., Nagatsuma, T. & Mittleman, D. M. Terahertz integrated electronic and hybrid electronic–photonic systems. *Nat. Electron.* **1**, 622–635 (2018).
17. Gu, Q. J. THz interconnect: the last centimeter communication. *IEEE Commun. Mag.* **53**, 206–215 (2015).
18. Liang, Y., Yu, H., Zhang, H. C., Yang, C. & Cui, T. J. On-chip sub-terahertz surface plasmon polariton transmission lines in CMOS. *Sci. Rep.* **5**, 14853 (2015).
19. Weissman, N., Jameson, S. & Socher, E. A packaged 106–110 GHz bi-directional 10Gbps 0.11 pJ/bit/cm CMOS transceiver. In *IEEE MTT-S International Microwave Symposium* 1–4 (IEEE, 2015).
20. Holloway, J. W., Boglione, L., Hancock, T. M. & Han, R. A fully integrated broadband sub-mm wave chip-to-chip interconnect. *IEEE Trans. Microw. Theory Tech.* **65**, 2373–2386 (2017).

21. Yu, B. et al. Ortho-mode sub-THz interconnect channel for planar chip-to-chip communications. *IEEE Trans. Microw. Theory Tech.* **66**, 1864–1873 (2017).
22. Ye, Y., Yu, B., Ding, X., Liu, X. & Gu, Q. J. High energy-efficiency high bandwidth-density sub-THz interconnect for the “last-centimeter” chip-to-chip communications. In *IEEE MTT-S International Microwave Symposium* 805–808 (IEEE, 2017).
23. Lu, L., Joannopoulos, J. D. & Soljačić, M. Topological photonics. *Nat. Photon.* **8**, 821–829 (2014).
24. Bahari, B., Tellez-Limon, R. & Kanté, B. Topological terahertz circuits using semiconductors. *Appl. Phys. Lett.* **109**, 143501 (2016).
25. Khanikaev, A. B. & Shvets, G. Two-dimensional topological photonics. *Nat. Photon.* **11**, 763–773 (2017).
26. Takata, K. & Notomi, M. Photonic topological insulating phase induced solely by gain and loss. *Phys. Rev. Lett.* **121**, 213902 (2018).
27. Ozawa, T. et al. Topological photonics. *Rev. Mod. Phys.* **91**, 015006 (2019).
28. Hafezi, M., Mittal, S., Fan, J., Migdall, A. & Taylor, J. Imaging topological edge states in silicon photonics. *Nat. Photon.* **7**, 1001–1005 (2013).
29. Chen, W.-J. et al. Experimental realization of photonic topological insulator in a uniaxial metacrystal waveguide. *Nat. Commun.* **5**, 5782 (2014).
30. Wu, L. H. & Hu, X. Scheme for achieving a topological photonic crystal by using dielectric material. *Phys. Rev. Lett.* **114**, 223901 (2015).
31. Cheng, X. et al. Robust reconfigurable electromagnetic pathways within a photonic topological insulator. *Nat. Mater.* **15**, 542–548 (2016).
32. Yves, S. et al. Crystalline metamaterials for topological properties at subwavelength scales. *Nat. Commun.* **8**, 16023 (2017).
33. Ma, T. & Shvets, G. All-Si valley-Hall photonic topological insulator. *New J. Phys.* **18**, 025012 (2016).
34. Wu, X. et al. Direct observation of valley-polarized topological edge states in designer surface plasmon crystals. *Nat. Commun.* **8**, 1304 (2017).
35. Dong, J. W., Chen, X. D., Zhu, H., Wang, Y. & Zhang, X. Valley photonic crystals for control of spin and topology. *Nat. Mater.* **16**, 298–302 (2017).
36. Gao, F. et al. Topologically protected refraction of robust kink states in valley photonic crystals. *Nat. Phys.* **14**, 140–144 (2018).
37. Noh, J., Huang, S., Chen, K. P. & Rechtsman, M. C. Observation of photonic topological valley Hall edge states. *Phys. Rev. Lett.* **120**, 063902 (2018).
38. Shalaev, M. I., Walasik, W., Tsukernik, A., Xu, Y. & Litchinitser, N. M. Robust topologically protected transport in photonic crystals at telecommunication wavelengths. *Nat. Nanotechnol.* **14**, 31–34 (2019).
39. He, X.-T. et al. A silicon-on-insulator slab for topological valley transport. *Nat. Commun.* **10**, 872 (2019).
40. Wang, Z., Chong, Y., Joannopoulos, J. D. & Soljačić, M. Observation of unidirectional backscattering-immune topological electromagnetic states. *Nature* **461**, 772–775 (2009).
41. Barik, S. et al. A topological quantum optics interface. *Science* **359**, 666–668 (2018).
42. Mittal, S., Goldschmidt, E. A. & Hafezi, M. A topological source of quantum light. *Nature* **561**, 502–506 (2018).
43. Bahari, B. et al. Nonreciprocal lasing in topological cavities of arbitrary geometries. *Science* **358**, 636–640 (2017).
44. Bandres, M. A. et al. Topological insulator laser: experiments. *Science* **359**, eaar4005 (2018).
45. Ota, Y., Katsumi, R., Watanabe, K., Iwamoto, S. & Arakawa, Y. Topological photonic crystal nanocavity laser. *Commun. Phys.* **1**, 86 (2018).
46. Hafezi, M., Demler, E. A., Lukin, M. D. & Taylor, J. M. Robust optical delay lines with topological protection. *Nat. Phys.* **7**, 907–912 (2011).
47. Yang, Y. et al. Realization of a three-dimensional photonic topological insulator. *Nature* **565**, 622–626 (2019).
48. Rechtsman, M. C. et al. Photonic Floquet topological insulators. *Nature* **496**, 196–200 (2013).
49. Barik, S., Miyake, H., DeGottardi, W., Waks, E. & Hafezi, M. Two-dimensionally confined topological edge states in photonic crystals. *New J. Phys.* **18**, 113013 (2016).
50. Lu, J. et al. Observation of topological valley transport of sound in sonic crystals. *Nat. Phys.* **13**, 369–374 (2017).
51. Knight, J., Birks, T., Russell, P. S. J. & Atkin, D. All-silica single-mode optical fiber with photonic crystal cladding. *Opt. Lett.* **21**, 1547–1549 (1996).
52. Barik, S. & Hafezi, M. Robust and compact waveguides. *Nat. Nanotechnol.* **14**, 8–9 (2019).
53. Koenig, S. et al. Wireless sub-THz communication system with high data rate. *Nat. Photon.* **7**, 977–981 (2013).
54. Zhang, Z. et al. Directional acoustic antennas based on valley-Hall topological insulators. *Adv. Mater.* **30**, 1803229 (2018).
55. Lu, L. et al. Experimental observation of Weyl points. *Science* **349**, 622–624 (2015).
56. Noh, J. et al. Experimental observation of optical Weyl points and Fermi arc-like surface states. *Nat. Phys.* **13**, 611–617 (2017).
57. Yang, B. et al. Ideal Weyl points and helicoid surface states in artificial photonic crystal structures. *Science* **359**, 1013–1016 (2018).

Methods

Effective Hamiltonian. For the VPC, its band around the K (K′) valley can be described by an effective massive two-dimensional Dirac Hamiltonian based on $k\cdot p$ theory[34,36,37,50]

$$H = v_{\mathrm{D}}\left(\delta k_x \sigma_x + \delta k_y \sigma_y\right) + v_{\mathrm{D}} m \sigma_z$$

where δk_x and δk_y are the momentum deviation from the K and K′ points, respectively, v_{D} is the group velocity of the Dirac cone, σ are Pauli matrices and m is the effective mass term related to the inversion-symmetry breaking. Topological kink states emerge at the boundary between two VPCs with opposite effective mass terms. The boundary is a Dirac mass domain wall, where a soliton-like state is localized. According to the Jackiw–Rebbi theory[58], one can derive the dispersions of kink states, which are $\delta\omega = v_{\mathrm{D}}\delta_k$ ($\delta\omega = -v_{\mathrm{D}}\delta_k$) centred at the projections of the K (K′) valley on the boundary[50]. Interestingly, the dispersion of the kink states is linear.

Sample fabrication. The dimensions of the triangular holes in THz VPC are comparable to those in silicon microelectromechanical systems (MEMS). Therefore, we employed photolithography and deep reactive ion etching in a MEMS foundry to fabricate a sample from high-resistivity (>10 kΩ cm) 4 inch silicon wafer[10]. The THz VPC is also compatible with a silicon-on-insulator platform. Furthermore, compact electronic sources and detectors such as THz resonant tunnelling diodes[59] can be readily integrated with our VPC waveguides for on-chip communication.

THz spectroscopy. A continuous-wave source is produced by a combination of a millimetre-wave signal generator and a ninefold frequency multiplier. A WR-3 hollow waveguide and a 3-mm-long tapered structure integrated with VPC samples are used to couple the THz wave efficiently into the domain wall. The positions of the sample and the WR-3 waveguide are carefully controlled using a micromechanical positioner. The output from the domain wall is down-converted to a 404.4 MHz IF signal by mixing with the LO signal generated from the spectrum analyser. To obtain the calibration data, two WR-3 waveguides without samples are directly connected to measure the output power. The samples are measured several times, and each transmission spectrum is plotted with its standard deviation to account for the uncertainties.

THz communication experiment setup. On the transmitter side of the THz communication system, a beating optical signal from two continuous-wave laser diodes is modulated using on–off keying by a pseudo-random bit stream, and then down-converted to THz frequencies via a UTC-PD[11]. This UTC-PD extracts the THz range beat frequency via envelope detection. The signal is transmitted across the VPC waveguide and is detected using a Schottky barrier diode with a bias voltage. The detected signal is amplified by a low-noise amplifier with bandwidth of 18 GHz and sharpened by a limiting amplifier. The eye diagram is observed on the screen of the oscilloscope. The bit error rate is measured using a bit-error-rate tester.

4K video transmission experiment setup. In the experiment, we use a 4K recorder (HyperDeck Studio Pro by Blackmagic Design) as the signal source that provides an uncompressed 4K video signal ('Seas of Ogasawara' 2160p30 format by Astrodesign) at a data transfer rate of 6 Gbit s^{-1}. The signal is transmitted through the VPC sample, and both the received and rectified signals are conditioned using an amplifier. A converter (Blackmagic Design) is used to convert the 6G-SDI (serial digital interface) signal into an HDMI (high definition multimedia interface) signal, which was then fed to a television.

Numerical simulation. The bulk/edge band structure, mode profiles, and Berry curvature of the VPC are numerically obtained with a finite-element method solver (COMSOL Multiphysics RF Module; www.comsol.com). The simulations of the field distribution near the highly twisted domain wall are performed in the time domain solver of CST Microwave Studios (www.cst.com).

Data availability

The data that support the plots within this paper and other findings of this study are available from the corresponding author upon reasonable request.

References

58. Jackiw, R. & Rebbi, C. Solitons with fermion number 1/2. *Phys. Rev. D* **13**, 3398 (1976).
59. Nishida, Y. et al. Terahertz coherent receiver using a single resonant tunnelling diode. *Sci. Rep.* **9**, 18125 (2019).

Acknowledgements

We thank Z. Xu at Zhejiang University for discussions, and J. Kim and Y. Nishida at Rohm Co. Ltd. for their help with experiments. Y. Yang, P.P., B.Z. and R.S. acknowledge research funding support from the Singapore Ministry of Education (grant numbers MOE2017-T2-1-110, MOE2018-T2-1-022(S) and MOE2016-T3-1-006(S)) and the National Research Foundation (NRF), Singapore and Agence Nationale de la Recherche (ANR), France (grant number NRF2016-NRF-ANR004). Work at Osaka University is supported in part by the Core Research for Evolutional Science and Technology (CREST) programme of the Japan Science and Technology Agency (grant number JPMJCR1534), KAKENHI, Japan (grant number 17H01764).

Author contributions

Y. Yang created the design, performed theoretical analysis and simulations, and helped to write the manuscript. Y. Yamagami performed simulations, experiments and data analysis. X.Y. helped with the design and performed the experiments. P.P. helped with the experiment design and simulations. J.W. helped with the communication experiment and data analysis. B.Z. provided input on topological protection. M.F. planned and co-led the project, performed the data analysis, and helped to write the manuscript. T.N. guided the project and communication experiments. R.S. planned and led the project and helped to write the manuscript. All authors contributed to the manuscript.

Competing interests

The authors declare no competing interests.

Additional information

Supplementary information is available for this paper at https://doi.org/10.1038/s41566-020-0618-9.

Correspondence and requests for materials should be addressed to M.F. or R.S.

Reprints and permissions information is available at www.nature.com/reprints.